Water Science & Technology

Water Science & Technology Vol 85 No 9, 2639 doi: 10.2166/wst.2022.139

Construction of g-C_3N_4/Ag/TiO_2 Z-scheme photocatalyst and Its improved photocatalytic U(VI) reduction application in water

Yuelin Liu[a,b], Yilei Yuan[c], Shangyuan Ni[b], Jun Liu[d], Shuibo Xie[c,e,*] and Yingjiu Liu[c]

[a] Key Discipline Laboratory for National Defence for Biotechnology in Uranium Mining and Hydrometallurgy, University of South China, Hengyang 421001, China
[b] School of Civil Engineering, Hunan University of Technology, Zhuzhou 412007, China
[c] Hunan Province Key Laboratory of Pollution Control and Resources Reuse Technology, University of South China, Hengyang 421001, China
[d] Hunan Key Laboratory of Biomedical Nanomaterials and Devices, School of Life Science and Chemistry, Hunan University of Technology, Zhuzhou 412007, China
[e] School of Civil Engineering, University of South China, Hengyang 421001, China
*Corresponding author. E-mail: xiesbmr@263.net

SX, 0000-0002-0125-2897

ABSTRACT

The reduction of soluble U(VI) to insoluble U(IV) by photocatalytic technology is considered to be a valid method to remove U(VI) from water. Herein, g-C_3N_4/Ag/TiO_2 Z-scheme heterojunction was synthesized for photocatalytic U(VI) reduction application. The SEM, XRD and XPS characterization results showed that a ternary g-C_3N_4/Ag/TiO_2 composite photocatalyst was synthesized successfully. g-C_3N_4/Ag/TiO_2 exhibited excellent photocatalytic reduction performance for U(VI) under visible light irradiation. After 30 min irradiation, the removal rate of U(VI) was above 99%. XPS indicated that the majority of U(VI) on the surface of g-C_3N_4/Ag/TiO_2 was reduced to U(IV). In addition, the photocatalytic activity of g-C_3N_4/Ag/TiO_2 has been kept significantly after five rounds of experiments, indicating good stability. g-C_3N_4/Ag/TiO_2 exhibited better photocatalytic reduction of U(VI) under visible light irradiation, which is mainly ascribed to Z-scheme photocatalytic mechanism assisted by the LSPR effect (Local Surface Plasmon Resonance). Ag with plasmon resonance effect on the loading has a strong absorption of photon energy. In addition, an intermediate charge transfer channel is formed between Ag and the semiconductor to inhibit the combination of photogenerated electrons and holes, resulting in a significant increase in the photocatalytic activity of the photocatalyst. This idea has some significance in design of other composite photocatalytic systems.

Key words: g-C_3N_4, photocatalysis, TiO_2, U(VI) reduction, Z-scheme

HIGHLIGHTS

- Z-scheme heterojunction was synthesized successfully.
- g-C_3N_4/Ag/TiO_2 exhibited excellent photocatalytic reduction performance for U(VI) under visible light irradiation.
- g-C_3N_4/Ag/TiO_2 exhibited better photocatalytic reduction of U(VI) under visible light irradiation, which is mainly ascribed to Z-scheme photocatalytic mechanism assisted by the LSPR effect.

1. INTRODUCTION

With the growth of the global energy crisis, nuclear energy is widely exploited and utilized. As a crucial nuclear energy fuel, uranium is widely applied in nuclear power generation, and it has grown over the century constantly (Carrara 2020). While nuclear energy is widely used, a large quantity of uranium-containing wastewater is created in the mining process, nuclear power plant operation process and nuclear accident leakage. Uranium-containing wastewater brings a severe risk to the environment because of its chemical and radiological toxicity (Liu *et al.* 2017a; Han *et al.* 2019). The uranium element in water is mainly in the form of hexavalent U(VI), which has good solubility and easy migration. The practical means to remove U(VI) from uranium-containing wastewater has become the research focus. Traditional methods (such as adsorption, evaporation, membrane separation, ion exchange) have some limitations and drawbacks (Heshmati *et al.* 2014; Guo *et al.* 2017; Torkabad *et al.* 2017; Taghipour *et al.* 2019; Yuan *et al.* 2020). Compared with these methods mentioned above, the reduction of soluble U(VI) to insoluble U(IV) has been considered as one of the valid approaches to solve this problem.

Among many reduction methods, photocatalysis is widely concerned because of its efficiency, green and no secondary pollution (Xu *et al.*, 2016, Khorsandi *et al.* 2019).

Some photocatalysts have been used to reduce U(VI). Such as TiO_2, graphitic carbon nitride (g-C_3N_4), iron oxide (α-Fe_3O_4), ZnO and so on (Guo *et al.* 2016; Guo *et al.* 2017; Wen *et al.* 2017, Lassoued *et al.* 2018; Liu *et al.* 2019; Liu *et al.* 2020). As the most classical photocatalyst, TiO_2 has been widely concerned because of its high activity and stability (Yu *et al.* 2014). Zhang *et al.* synthesized rutile TiO_2 nanorods for the photocatalytic reduction of U(VI), which obtained gratifying results (Zhang *et al.* 2013). Li *et al.* extracted uranium from seawater by photocatalytic reaction of TiO_2 (Li *et al.* 2019). However, the unsatisfactory visible light responsiveness of TiO_2 restricted its further applications (Almeida *et al.* 2022). g-C_3N_4 is a new research focus in photocatalysis due to its advantages such as proper band gap, high photocatalytic activity and no environmental contamination. Lu *et al.* has achieved satisfactory results in U(VI) reduction with a photocatalyst based on g-C_3N_4 (Lu *et al.* 2016; Lu *et al.* 2017). Nevertheless, the photocatalytic activity of pristine g-C_3N_4 is unsatisfactory because of its high recombination of photo-produced electrons and holes (Wen *et al.* 2017; Wang *et al.* 2018). Construction of heterojunction is considered as one of the effective ways to solve the above shortcomings of single component photocatalyst (Wang *et al.* 2020). Z-scheme heterojunction photocatalysts showed excellent photocatalytic activity because they could effectively separate electrons and holes produced by light, thus inhibiting their recombination (Tian *et al.* 2015; Ma *et al.* 2017; Liu *et al.* 2017b; ; Mao *et al.* 2018). There are a large number of reports about Z-scheme photocatalysts used to treat pollutants in aqueous (Zhu *et al.* 2016; Chen *et al.* 2019). In recent years, some literatures have reported the photocatalytic reduction of U(VI). However, this research is still at its primary stage compared with other applications, such as photocatalytic CO_2 reduction, water splitting, heavy metals treatment and organic pollutants degradation (Ping *et al.* 2019). Recently, Z-scheme g-C_3N_4/TiO_2 photocatalyst has been applied in reduction of U(VI), which has achieved gratifying results, Jiang *et al.* reported that g-C_3N_4/TiO_2 showed excellent photocatalytic property of U(VI) reduction and As(III) oxidation under simulated sunlight irradiation (Jiang *et al.* 2018). The preliminary study of our research group found that g-C_3N_4/TiO_2 had significant photocatalytic effect on U(VI) reduction under ultraviolet light irradiation (Liu *et al.* 2021). Dai *et al.* reported that $ZnFe_2O_4$/g-C_3N_4 could efficient removal of U(VI) via simultaneous adsorption and photoreduction under visible LED light irradiation (Dai *et al.* 2021). Adding a noble metal into a semiconductor is one of the effective means to improve their photocatalytic performance. The Fermi level of a noble metal is usually less than that of semiconductor photocatalytic material, when the noble metal is deposited on the photocatalytic material, electrons can be rapidly transferred from the semiconductor photocatalytic material to the noble metal material, so that the overall Fermi level of the material can reach the level of noble metal (Link *et al.* 2011; Guo *et al.* 2013; Bian *et al.* 2014). Tada *et al.* modified TiO_2 by Ag deposition, and the results showed that supporting a small amount of Ag could significantly improve the activity of TiO_2 photocatalytic reduction of nitrobenzene (Tada *et al.* 2004). According to the current reports, photocatalytic reduction of U(VI) employing Z-scheme photocatalysts is still an innovative method. In addition, it is also necessary to further study this photocatalytic process and its corresponding mechanism in reduction of U(VI).

Herein, g-C_3N_4/Ag/TiO_2 nanocomposites were synthesized and characterized by scanning electron microscope (SEM), X-ray diffraction and X-ray electron spectroscopy (XPS) in this work. The as-synthesized g-C_3N_4/Ag/TiO_2 was applied for efficient reduction of U(VI) via photochemical reaction under visible light irradiation. The Z-scheme photocatalytic mechanism of g-C_3N_4/Ag/TiO_2 has been researched, which could cut down the recombination of photogenerated electrons and holes. More significantly, the role of Ag has been investigated, which could increase the light absorption range of photocatalysts. In this study, an all-solid Z-scheme photocatalytic system was constructed, and the principle of fast separation of carriers was used to promote the participation of electrons on the surface of g-C_3N_4 in U(VI) reduction and improve the photocatalytic efficiency.

2. EXPERIMENTAL

2.1. Preparation of material

The g-C_3N_4/Ag/TiO_2 was synthesized reference to patent (Wu 2013) and some adjustments were made to the synthesis process.

All chemical reagents were domestic reagents, which were at analytic grade without further purification. P25 was used as the source of TiO_2, and it was purchased from King chemical. U_3O_8 (99%) was dissolved by HCl and H_2O_2 under heating conditions for standard U(VI) solution. An appropriate amount of melamine was weighed into a porcelain crucible and

placed in a muffle roaster. The temperature of the muffle furnace was kept at 540 °C for 2 h and so cooled down naturally. After cooling to room temperature, the sample was weighed and ground into powder form to obtain the light yellow photocatalyst g-C_3N_4.

100 g g-C_3N_4 powder and 4 g P25 (TiO_2) was added into anhydrous ethanol solution and then sonicated (40,000 Hz) in a water bath for 15 min until the powder was utterly dispersed (keep stirring throughout the process). The g-C_3N_4 powder was evaporated by vacuum drying at 80 °C for 5 h. After grinding, the powder was forged in a muffle furnace at 400 °C for 2 h to cool down naturally. After cooling to room temperature and removing, the sample was weighed and ground into powder form to obtain binary composite photocatalyst g-C_3N_4/TiO_2.

0.1 g g-C_3N_4/TiO_2 and 0.5 g aminopropyl trimethoxysilane were dispersed in 20 ml ethanol and stirred for 8 h (the amount of ethanol does not need to be strictly controlled, as long as g-C_3N_4/TiO_2 could be utterly dispersed). The separation was washed for three times after it was separated by centrifugation. The resulting solid was dispersed in 20 ml ethanol again. 0.5 g $AgNO_3$ was added and stirred for 2 h. After centrifugation, it was dispersed in water. A small amount of $NaBH_4$ was added. The above suspension was dried at 80 °C for 5 h, the photocatalyst g-C_3N_4/Ag/TiO_2 was prepared.

2.2. Characterization

2.2.1. SEM

The surface morphology of the samples was analyzed and measured using a Sigma 300 high-resolution scanning electron microscope (acceleration voltage 0.2–30 KV, INLENS and ET secondary electron detector imaging and EDS energy spectrometer, electromagnetic/electrostatic compound lens for objective lens, resolution 1.0 nm@15 kV, 1.6 nm@1 kV) from Zeiss, Germany.

2.2.2. XRD

The crystal structure and surface chemical composition of the samples were determined using a D/MAX-RB X-ray diffractometer (Cu Kα excitation source, scanning range 5°–90°, scanning rate 10°/min) from Bruker, Germany.

2.2.3. XPS

An X-ray electron spectrometer (ESCALAB 250Xi, Thermo Fischer, USA) with a vacuum of 8xl0-10 Pa, an Al ka-ray excitation source (hv = 1486.6 eV), an operating voltage of 12.5 kV, a filament current of 16 mA, and 10 cycles of signal accumulation was used. The test passing energy was 50 ev for the full spectrum, 20 eV for the narrow spectrum with a step of 0.05 eV, dwell time of 40–50 ms, and charge correction with C1 s = 284.80 eV binding energy as the energy standard) was used to analyze the surface elements and valence states of the samples.

2.2.4. Ultraviolet-visible diffuse reflectance spectroscopy (UV-vis DRS)

The UV-vis diffuse reflectance spectrometer UV-3600 (with integrating sphere device) of Shimadzu Corporation, Japan, was used to measure the light absorption properties of the samples.

2.2.5. Fluorescence spectrophotometer (PL)

The fluorescence spectra of the samples were measured using a fluorescence spectrophotometer of Edinburgh, UK, model FLS1000 with a xenon lamp as the excitation source (375 nm).

2.3. Photocatalytic activities of photocatalysts

The photocatalytic activities of the as-obtained photocatalysts were evaluated by the photocatalytic reduction of U(VI). In the photocatalytic process, 0.02 g of photocatalysts (TiO_2, g-C_3N_4, g-C_3N_4/TiO_2, g-C_3N_4/Ag/TiO_2) were added into 50 mL of uranium solution with an initial concentration of 10 mg/L, and 2 mL of methanol was added, which played the hole trapping agent. The pH was adjusted to 5 with HCl and NaOH. The suspension was stirred well for 30 min to allow the photocatalyst to be completely and uniformly dispersed in the suspension. The photocatalyst was first dark-reacted for 30 min to allow the photocatalyst to reach equilibrium for the adsorption of U(VI) in the solution, after which the photoreaction was carried out under 500 W xenon lamp irradiation. The remaining U(VI) concentration in the supernatant was measured after centrifugation of samples at certain intervals. Nitrogen was introduced throughout the whole reaction process to eliminate the influence of dissolved oxygen on the test. The photocatalytic test is applied within the photocatalytic equipment. Arsenazo III spectrophotometric methodology determined the U(VI) concentration of suspension after centrifugation at regular

intervals. The following expression calculated the removal ratios ($R_{U(VI)}$) of U(VI):

$$R_{U(VI)} = (1 - C_t/C_0) \times 100\% = (A_0 - A_t)/A_0 \times 100\%$$

$R_{U(VI)}$ are removal ratios of U(VI), C_t and C_0 are concentration of U(VI) at 0 and t time, A_0 and A_t are absorbance intensity corresponding to 0 and t time, respectively. The stability of g-C_3N_4/Ag/TiO_2 was evaluated by reusing the photocatalyst in five recurrent tests for reduction of U(VI) underneath constant conditions.

3. RESULTS AND DISCUSSION

3.1. Morphological analysis

The morphologies of g-C_3N_4, TiO_2, g-C_3N_4/TiO_2, and g-C_3N_4/Ag/TiO_2 were characterized by SEM, and the results are shown in Figure 1. From Figure 1(a), it can be seen that the g-C_3N_4 is presented with a bulk structure consisting of many irregularly shaped wrinkled sheets aggregated. A magnified SEM image of g-C_3N_4 is shown in Figure 1(b), in which it can be clearly seen that the g-C_3N_4 has a block structure with holes. These cavities can effectively increase the specific surface area of g-C_3N_4 and provide more reactive sites for photocatalytic reactions. The SEM images of pure TiO_2(P25) are shown in Figure 1(c) and 1(d). It can be seen from the images that TiO_2 is an irregular spherical particle with particle size less than 100 nm, which is much smaller than g-C_3N_4. The SEM images of the binary composite g-C_3N_4/TiO_2 are shown in Figure 1(e) and 1(f). It can be seen in the images that TiO_2 nanoparticles are uniformly attached to the surface of g-C_3N_4. There is no obvious exposed g-C_3N_4 surface in these SEM images. Figures 1(g) and 1(h) show the SEM images of the ternary composite g-C_3N_4/Ag/TiO_2. In Figure 1(g), it can be seen that a large number of irregular spherical particles are uniformly attached to the surface of the bulk g-C_3N_4, and no obvious exposed outer surface of g-C_3N_4 is seen in the images. The magnified g-C_3N_4/Ag/TiO_2 SEM image is shown in Figure 1(h); it is evident that there are two particles of different sizes present on the surface of g-C_3N_4. From the analysis of the particle number ratio and the size of TiO_2 particles in Figure 1(f), it is inferred that the larger particle on the outer surface of g-C_3N_4 in Figure 1(h) is Ag nanoparticles. The SEM results indicate that the ternary g-C_3N_4/Ag/TiO_2 composite photocatalyst was successfully prepared.

3.2. XRD analysis

The crystal structures of TiO_2, g-C_3N_4, g-C_3N_4/TiO_2, and g-C_3N_4/Ag/TiO_2 were characterized by XRD, and the results are shown in Figure 2. The red line in the figure is the XRD pattern of g-C_3N_4, and it can be seen that the significant characteristic peaks appear at two positions, 13.1° and 27.3°, comparable to the (100) and (002) crystal planes of g-C_3N_4, severally. This result indicates that the prepared g-C_3N_4 has multiple honeycombs and stacked structures within the facets. The weak diffraction peak signal at 13.1° indicates that the prepared g-C_3N_4 has a graphene structure. The blue line is the XRD pattern of g-C_3N_4/TiO_2. The intensity of the significant peak of g-C_3N_4 is reduced due to the high proportion of TiO_2 in g-C_3N_4/TiO_2. The diffraction peaks of both anatase TiO_2 and rutile TiO_2 appear in the nanostructure of g-C_3N_4/TiO_2. Most of the diffraction peaks are characteristic peaks of anatase TiO_2 (Liu *et al.* 2015), including (101), (004), (200), (105), (211), (204), (116), (220) and (215). The remaining (110), (101), (111) and (220) are characteristic peaks of rutile TiO_2, and the corresponding characteristic peaks are consistent with those of pure P25 (black lines). The pink line in the XRD pattern is belonging to g-C_3N_4/Ag/TiO_2. It can be seen that the pink line is almost the same as the blue line of g-C_3N_4/TiO_2 sample, and no significant characteristic peak of Ag is shown. This is probably because the proportion of Ag in g-C_3N_4/Ag/TiO_2 is too low to detect. A similar phenomenon was appeared in the XRD characterization of the photocatalyst Ag/2D-C_3N_4 prepared by Yi *et al.* (2016).

3.3. XPS analysis

In order to further verify the presentation of Ag in g-C_3N_4/Ag/TiO_2, the elemental analysis of g-C_3N_4/Ag/TiO_2 was performed by XPS characterization, and the results are shown in Figure 3. Figure 3(a) reveals the XPS full spectrum of g-C_3N_4/Ag/TiO_2, which contains the characteristic peaks of C 1 s, N 1 s, Ti 2p, O 1 s and Ag 3d. Figure 3(b) shows the high-resolution XPS spectrum of Ti 2p in g-C_3N_4/Ag/TiO_2, and the positions of the two characteristic peaks of Ti 2p3/2 and Ti 2p1/2 in.the spectrum indicate that the element Ti exists in g-C_3N_4/Ag/TiO_2 in the form of Ti^{4+}. Figure 3(c) shows the high-resolution XPS spectra of C1 s in g-C_3N_4/Ag/TiO_2. The characteristic peaks of C1 s at two positions, 284.8 eV and 288.0 eV, can be seen due to the coordination bonds of aromatic hydrocarbon carbon atoms and C-N-C, respectively. Figure 3(d) shows two

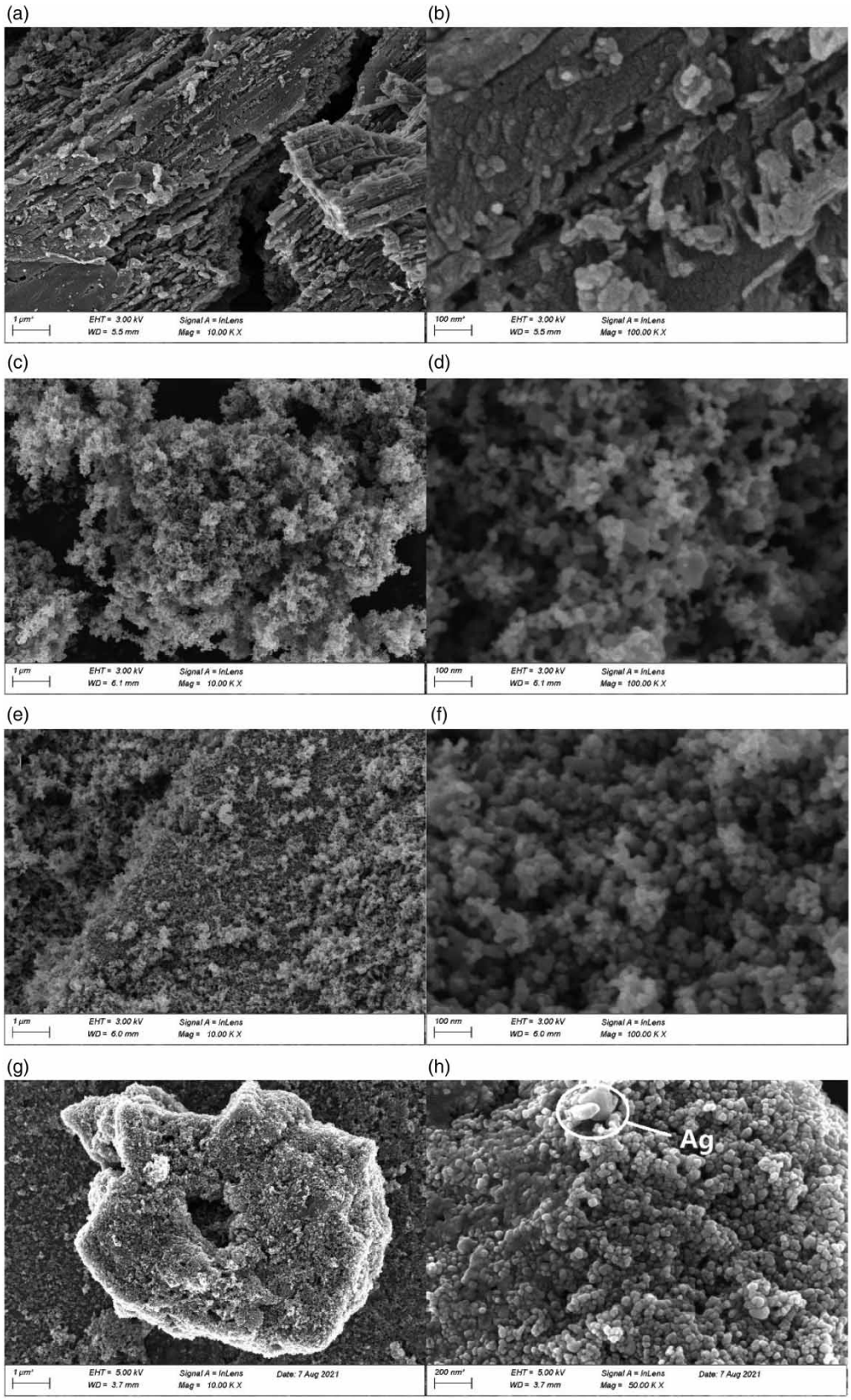

Figure 1 | SEM of pure g-C_3N_4 (a, b), TiO_2 (P25, c, d), g-C_3N_4/TiO_2 nanostructures (e, f) and g-C_3N_4/Ag/TiO_2 (g, h).

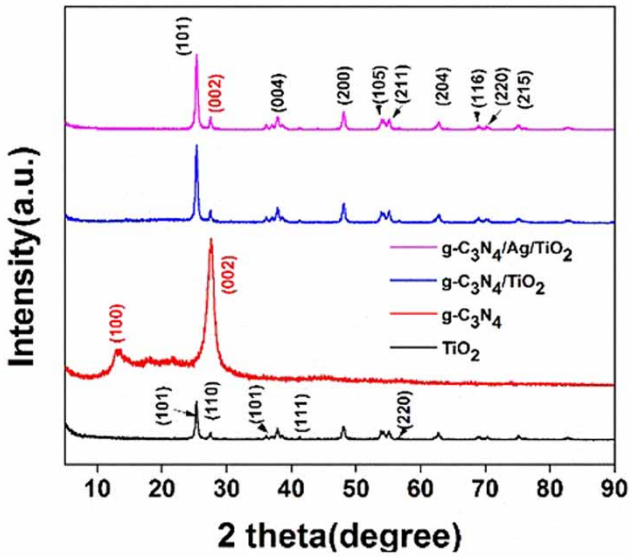

Figure 2 | XRD patterns of as-prepared g-C_3N_4, TiO_2, g-C_3N_4/TiO_2 and g-C_3N_4/Ag/TiO_2 samples.

high-resolution XPS peaks at 398.5 eV and 400.4 eV of N 1 s in g-C_3N_4/Ag/TiO_2, which could be ascribed to the coordination bonds of C-*N* = C and C-N-H, respectively. Figure 3(e) shows the high-resolution XPS spectrum of O 1 s in g-C_3N_4/Ag/TiO_2, which shows the characteristic peak of O 1 s formed only at 530.1 eV, indicating that O exists only in the valence state of O^{2-} in g-C_3N_4/Ag/TiO_2. This result matches the morphology of O^{2-} in TiO_2, indicating that both Ti and O elements exist in the sample in the form of TiO_2. Figure 3(f) shows the high-resolution XPS spectrum of Ag 3d in g-C_3N_4/Ag/TiO_2, in which it can be seen that Ag 3d appears as characteristic peaks at 367.8 eV and 373.8 eV, respectively. An energy difference of ~6.0 eV between these two peaks, indicating the presence of Ag in g-C_3N_4/Ag/TiO_2 in the form of singlet silver. The XPS results further indicate that the composite photocatalyst g-C_3N_4/Ag/TiO_2 was synthesized successfully, in which Ag exists in the form of elemental silver.

3.4. Optical properties analysis

The light absorption properties of TiO_2, g-C_3N_4, g-C_3N_4/TiO_2, and g-C_3N_4/Ag/TiO_2 were analyzed by UV-vis diffuse reflection factor spectroscopic analysis (DRS). The results are shown in Figure 4(a). In this figure, the light absorption area of TiO_2 was represented by the red line, which is mainly concentrated in the UV region, with the absorption sideband at ~400 nm. The blue line represents g-C_3N_4 which is able to response light at lower frequency wavelengths compared to TiO_2, with the absorption sideband at ~450 nm, indicating that g-C_3N_4 has a certain responsiveness to visible light at wavelengths above 420 nm. The yellow line represents the absorption sideband of g-C_3N_4/TiO_2, which is very close to that of g-C_3N_4 also at ~450 nm. g-C_3N_4/TiO_2 has a lower absorption ability than TiO_2 in the UV region but higher than g-C_3N_4, indicating that the composite g-C_3N_4/TiO_2 photocatalyst was synthesized successfully. The absorption ability of g-C_3N_4/Ag/TiO_2 in the UV region represented by the green line is higher than that of the other three materials. An obvious surface plasmon resonance absorption peak of silver nanoparticles located at ~450 nm appears, which makes the absorption intensity of g-C_3N_4/Ag/TiO_2 in the visible area significantly enhanced (red arrow in the figure). In addition, the bandgap energies of TiO_2, g-C_3N_4, g-C_3N_4/TiO_2, and g-C_3N_4/Ag/TiO_2 were extrapolated based on the plot of $(ahv)^2$ versus hv, and the results are shown in Figure 4(b). The band gap energies (E_g) of g-C_3N_4, TiO_2, g-C_3N_4/TiO_2, and g-C_3N_4/Ag/TiO_2 were calculated to be 2.7 eV, 3.2 eV, 2.8 eV and 2.25 eV respectively. Figure 4 illustrated that the absorption performance of g-C_3N_4/Ag/TiO_2 for light is enhanced after loading with Ag, especially in the visible region.

The efficiency of photogenerated electron-hole separation in g-C_3N_4, TiO_2, g-C_3N_4/TiO_2, and g-C_3N_4/Ag/TiO_2 under illumination conditions was examined by PL. The photogenerated electron-hole recombination releases energy in the form of PL emission. Therefore, the PL intensity is directly related to the recombination rate of photogenerated electrons with holes. PL spectra of g-C_3N_4, TiO_2, g-C_3N_4/TiO_2, and g-C_3N_4/Ag/TiO_2 are shown in Figure 5. Among them, for g-C_3N_4 and TiO_2 (the black line and pink line), the PL spectrum has a strong emission peak at ~460 nm, indicating the presence of a large number

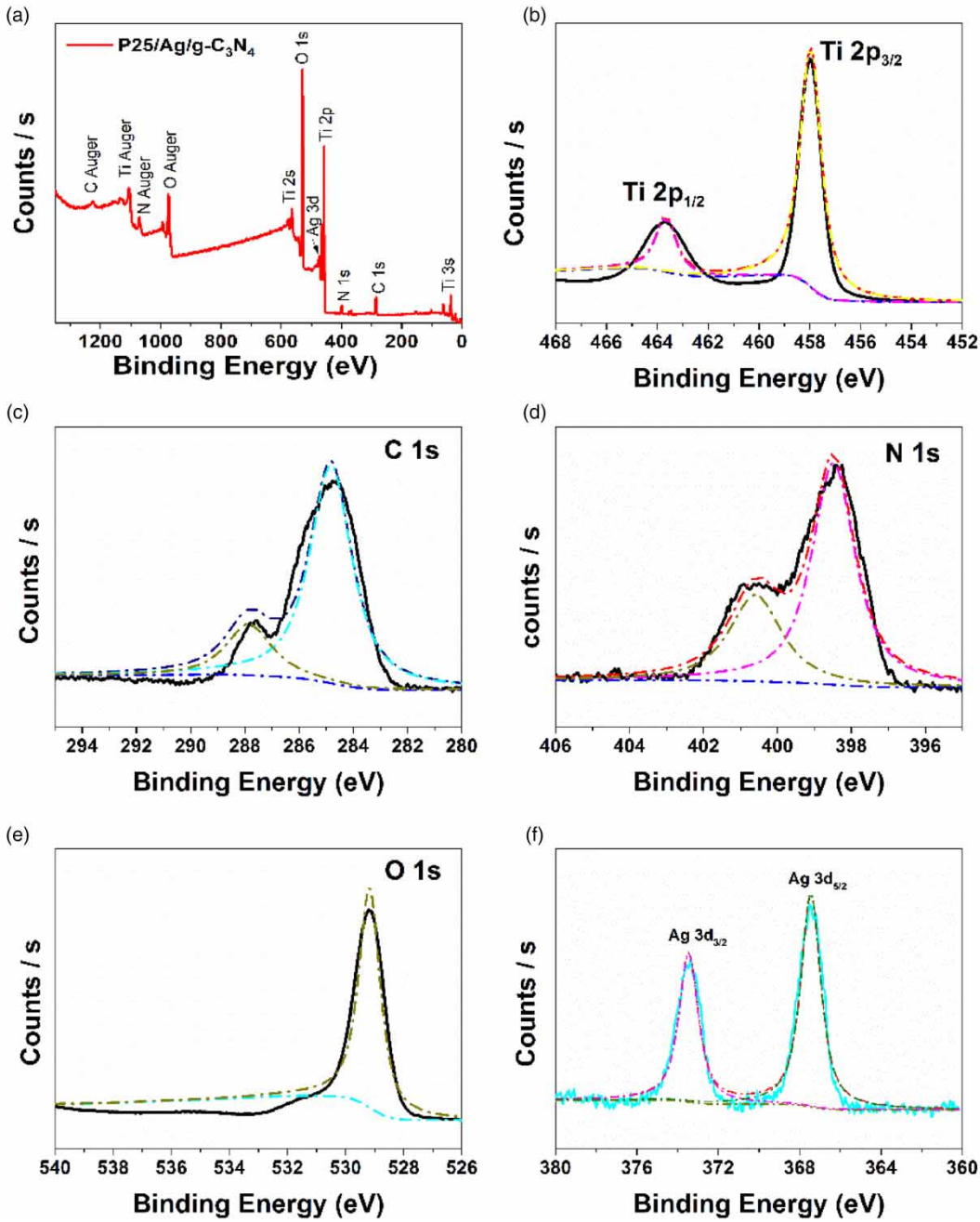

Figure 3 | (a) the complete XPS spectra of g-C_3N_4 Ag/TiO_2, main peaks of Ti 2p (b), C 1 s (c), N 1 s (d), O 1 s (e) and Ag 3d (f) for g-C_3N_4/TiO_2.

of photo-generated electrons recombined with holes. A large amount of energy was discharged throughout the recombination process may well be detected by the PL spectrum. For g-C_3N_4/TiO_2 represented by the red line, there is a weaker emission peak at ~430 nm in the PL spectrum, indicating the presence of a small number combination of photogenerated electrons and holes, because the Z-scheme structure of the composite photocatalyst g-C_3N_4/TiO_2 effectively reduces the photogenerated electron-hole recombination rate. For the g-C_3N_4/Ag/TiO_2 represented by the blue line, there is no obvious emission peak in the PL spectrum, indicating that the Ag-loaded g-C_3N_4/Ag/TiO_2 further reduces the photogenerated electron-hole recombination rate because the good conductivity of Ag makes the photogenerated electrons migrate in a directional manner. Meanwhile, the space charge layer formed between Ag, g-C_3N_4 and TiO_2 also plays a role in suppressing the recombination of photogenerated electrons and holes.

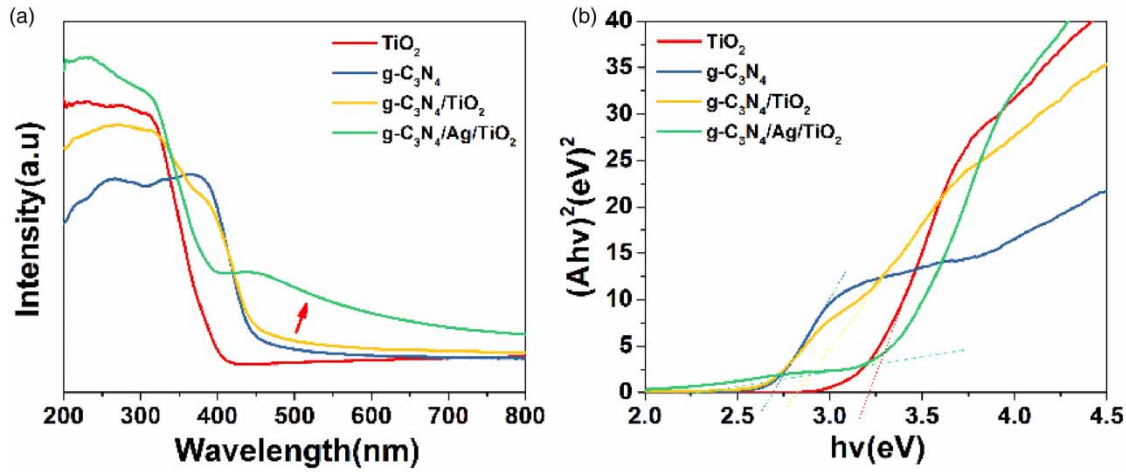

Figure 4 | (a) UV-vis diffuse reflectance spectra of pure g-C_3N_4, TiO_2 (P25), g-C_3N_4/TiO_2 and g-C_3N_4/Ag/TiO_2 nanostructures; (b) plots of the $(Ahv)^2$ versus hv for pure g-C_3N_4, TiO_2 (P25) g-C_3N_4/TiO_2 and g-C_3N_4/Ag/TiO_2 nanostructures.

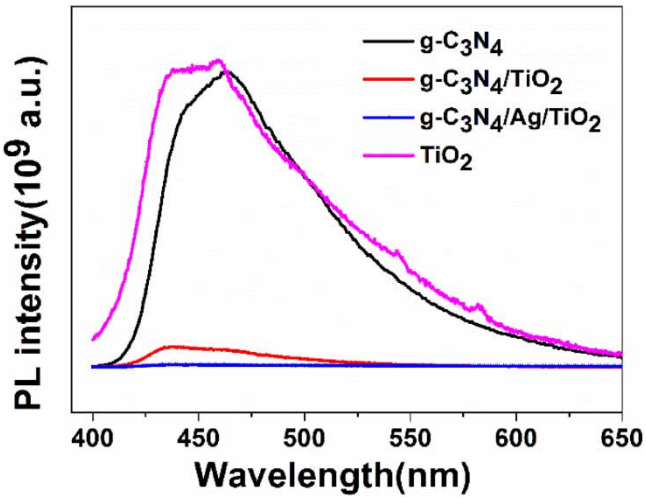

Figure 5 | PL spectra of g-C_3N_4, TiO_2, g-C_3N_4/TiO_2 and g-C_3N_4/Ag/TiO_2.

3.5. Photocatalytic reduction of U(VI)

The results of the photocatalytic reduction test are shown in Figure 6. The concentration of U(VI) did not change significantly under the light conditions without the injection of the photocatalyst, indicating that U(VI) was stable under light and the self-photocatalytic process could be ignored. Under the conditions of photocatalysts (g-C_3N_4, TiO_2, g-C_3N_4/TiO_2, g-C_3N_4/Ag/TiO_2) injection, the dark reaction was first allowed to reach adsorption equilibrium for 30 min, at which time the highest residual rate of U(VI) of the test group with g-C_3N_4 injection was close to 90%; the test group with TiO_2, g-C_3N_4/TiO_2, g-C_3N_4/Ag/TiO_2 were all-around 67% of the residual rate of U(VI). After the light source was turned on for the photoreaction, the remaining concentration of U(VI) in the test group with g-C_3N_4 injection decreased slowly, and the remaining rate of U(VI) was 80.8% after 30 min of photoreaction. The residual concentration of U(VI) in the test group with TiO_2 injection was decreased slowly, and the residual rate of U(VI) was 58.4% after 30 min of photoreaction. In the g-C_3N_4/TiO_2 group, the residual concentration of U(VI) decreased slightly faster than that of the TiO_2 group as the photoreaction proceeded, and the residual rate of U(VI) was 52.8% after 30 min of photoreaction. The concentration of U(VI) in the test group with g-C_3N_4/Ag/TiO_2 was decreased rapidly at the first 5 min of photoreaction. The concentration of U(VI) was also decreased gradually during the subsequent 25 min of photoreaction, and the residual rate of U(VI) was less than 1% at the end of the reaction (i.e., the removal rate was more than 99%).

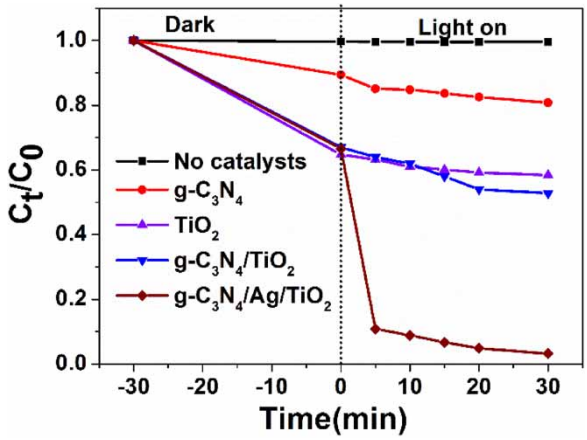

Figure 6 | The U(VI) residue rate varies with reaction.

The XPS spectra of U elements deposited on the g-C_3N_4/Ag/TiO_2 surface before and after the photocatalytic reaction were used to analyze the valence change of U elements during the photocatalytic reaction. Figure 7 shows the high-resolution XPS spectra of U4f before and after the photocatalytic reaction. It can be seen from the figure that the peak positions of U4f5/2 and 4f7/2 changed when U(VI) was reduced to U(IV). At the bottom of the red curve, four peaks were obtained at 379.6 eV, 381.9 eV, 390.4 eV and 391.3 eV, respectively, using the peak differentiation technique. Among them, the peaks at 381.9 eV and 391.3 eV belong to the U(VI) characteristic position, and the peaks at 379.6 eV and 390.4 eV belong to the U(IV) characteristic position. This indicates that the majority of the U(VI) on the g-C_3N_4/Ag/TiO_2 surface is reduced to U(IV) during the photoreaction. The process of U(VI) removal is not only the adsorption of the material, but also the process of valence change exists.

The stability of g-C_3N_4/Ag/TiO_2 photocatalytic reduction of U(VI) was investigated by a cycling test. After each cycle, the photocatalyst was separated from the suspension by centrifugation. The photocatalyst was stripped of its surface deposits by ultrasonic shaking and rinsed with deionized water. Subsequently, the photocatalyst was dried at 60 °C before the next cycle for the next use. The results of the cycling tests are shown in Figure 8. After five rounds of cycling tests, the photocatalytic activity of g-C_3N_4/Ag/TiO_2 did not decrease significantly. The final removal rate was still above 99%, which indicates that the photocatalytic activity of g-C_3N_4/Ag/TiO_2 remained stable after several cycles of reaction.

3.6. Reduction mechanisms of U(VI)

The main mechanism for the enhanced photocatalytic performance of g-C_3N_4/Ag/TiO_2 composite photocatalysts is the Z-scheme photocatalytic mechanism assisted by the LSPR effect. Combining noble metals with semiconductors could

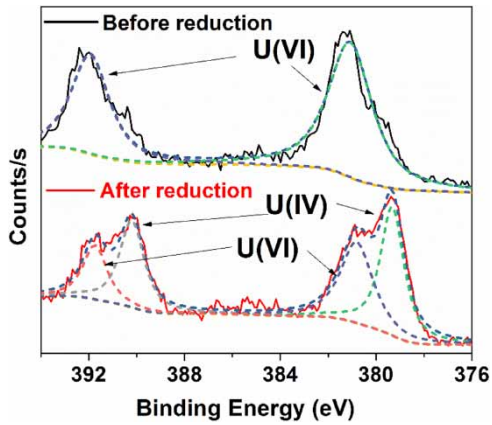

Figure 7 | XPS spectrum of U 4f for the U element on the surface of g-C_3N_4/Ag/TiO_2 before and after reduction process.

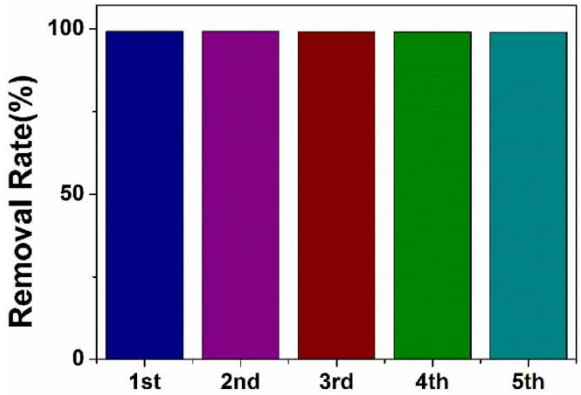

Figure 8 | Cyclic process of photocatalytic reduction of U(VI).

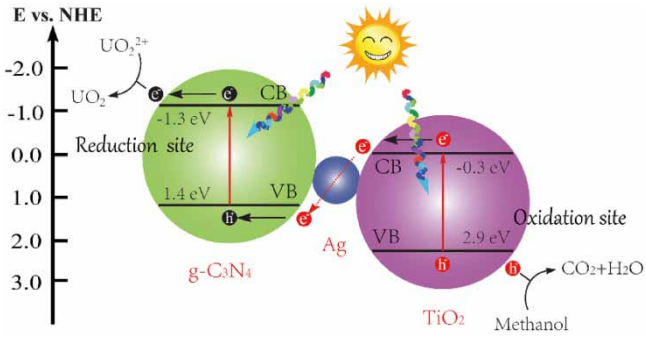

Figure 9 | The diagram of the proposed mechanism of g-C_3N_4/Ag/TiO_2 nanostructures under irradiation.

significantly promote the photocatalytic activity of semiconductors. Firstly, the LSPR effect of noble metal effectively promotes the separation of carriers, which is a kind of absorption effect of noble metals on photons: when the incident photon frequency matches the vibration frequency of conduction electrons of noble metal nanoparticles, the nanoparticles can produce strong absorption of photon energy (Tong *et al.* 2011). A part of such electrons injected from noble metal to semiconductor still retransmits to the Fermi energy level of the noble metal to compound with holes, which reduces the photocatalytic activity. In addition, too many of the electrons injected into the semiconductor do not have time to participate in the reaction before they were combined with the holes on the semiconductor, which is also an important factor in reducing the photocatalytic activity (Ingram & Linic 2011). Therefore, the appropriate amount of noble metal loading is required to improve the photocatalytic activity of semiconductors.

Figure 9 demonstrates the photocatalytic mechanism of g-C_3N_4/Ag/TiO_2 nanostructure under simulated solar (xenon lamp) irradiation. The bandgap energies of g-C_3N_4 and TiO_2 are 2.7 and 3.2 eV, respectively, relative to the standard hydrogen potential (Li & Ding 2010; Linic *et al.* 2011). The work function of Ag is 4.8 eV, and its position can be calculated as 0.3 eV relative to the standard hydrogen potential (Zhou *et al.* 2013). Under simulated sunlight irradiation, as shown in Figure 9, g-C_3N_4, TiO_2, and metallic Ag can all absorb light and generate photogenerated electron-hole pairs. Among them, the metal Ag can absorb visible light and thus be activated by the near-field enhancement effect of LSPR. In addition, the noble metal nanoparticles could generate a strong *in situ* surface electric field, which excites g-C_3N_4 and TiO_2 to produce more electron-hole pairs. The photogenerated electrons generated by metallic Ag move to the VB of TiO_2 for carrier combination with the holes. The excited electrons on the surface of g-C_3N_4 move to the metal Ag for the second carrier combination. The electrons on the CB of g-C_3N_4 can finally participate directly in the reduction of U(VI); while the holes left on the VB of TiO_2 can be trapped by methanol to produce CO_2 and H_2O. In this way, metal Ag served as a combination site for electrons and holes from different semiconductors. It is the main driving force for carrier separation on g-C_3N_4 and TiO_2. In addition, the noble metal Ag is a conductive material that can directly act as a centre to combine the electrons on the surface of TiO_2 with the holes on g-C_3N_4, ultimately forming a Z-scheme photocatalytic system.

In this way, the redox reaction happened on each semiconductor by their photogenerated electrons (g-C_3N_4) and holes (TiO_2). The recombination of photogenerated electrons and holes is effectively avoided, and therefore the photocatalytic performance is improved. Based on Marta's previous work (Litter 2017), the mechanism of U(VI) photocatalytic reduction is mainly as follows: in the first step, U(VI) is reduced to U(V) by photogenerated electrons. U(V) reacts spontaneously with U(VI) and U(IV), following the electron balance principle. Meanwhile U(V) can be further reduced to U(IV) by photogenerated electrons. And according to the one-step reduction theory of U(VI) (Lu *et al.* 2016), the reduction potential $E_0 = 0.411$ eV is required when U(VI) is directly reduced to U(IV) by one step in the presence of photogenerated electrons. As shown in Figure 9, the reduction potential of CB on g-C_3N_4 ($E_0 = -1.3$ eV) is more negative than the reduction potential required for a series of reactions. In theory, the photocatalytic reduction reaction can be carried out. Although g-C_3N_4 responds to visible light, as presented in Figure 5, the combination of photogenerated electron and hole was rather high. TiO_2 and g-C_3N_4/TiO_2 have a poor response to visible light (Figure 4). Therefore, the g-C_3N_4/Ag/TiO_2 exhibited better photocatalytic activity under the irradiation of visible light compared to pure g-C_3N_4, TiO_2 and g-C_3N_4/TiO_2 composition.

4. CONCLUSIONS

The ternary composite photocatalyst g-C_3N_4/Ag/TiO_2 was prepared by loading a small amount of the noble metal Ag. The characterization results showed that the ternary composite photocatalyst g-C_3N_4/Ag/TiO_2 was successfully prepared. g-C_3N_4/Ag/TiO_2 exhibited the best photocatalytic reduction performance for U(VI) under visible light irradiation. After 30 min irradiation, the removal rate of U(VI) was above 99%. By the XPS analysis of U elements deposited on the surface of g-C_3N_4/Ag/TiO_2 before and after the photocatalytic reaction, most of the U(VI) was reduced to U(IV). In addition, the photocatalytic activity of g-C_3N_4/Ag/TiO_2 did not decrease significantly after five rounds of experiments, showing its good stability. g-C_3N_4/Ag/TiO_2 exhibited better photocatalytic reduction of U(VI) under visible light irradiation mainly by the Z-scheme photocatalytic mechanism assisted by the LSPR effect. Although the introduction of noble metals will cause the price of photocatalyst preparation to increase, the increase in cost is not significant because of the small loading amount, and the overall cost performance is high. This idea has some significance in designing other photocatalytic materials.

ACKNOWLEDGEMENTS

The authors are grateful to the Laboratory of Pollution Control and Resource Technology and the Department of Municipal Engineering at the University of South China for providing the necessary facilities for the research. This research was funded by the National Natural Science Foundation of China (NO.11475080). Natural Science Foundation of Hunan Province (No.2019JJ50127).

AUTHOR CONTRIBUTION

Yuelin Liu contributed to the conception and design of the study. Yilei Yuan and Shangyuan Ni contributed to the acquisition of data. Yuelin Liu and Jun Liu contributed to analysis and interpretation of data. Yuelin Liu contributed to drafting the manuscript. Shuibo Xie and Jun Liu contributed to revising it critically for important intellectual content. Shuibo Xie and Yingjiu Liu contributed to the reagents/materials/analysis tools.

CONFLICTS OF INTEREST

The authors declare no conflict of interest.

DATA AVAILABILITY STATEMENT

Data cannot be made publicly available; readers should contact the corresponding author for details.

REFERENCE

Almeida, G., Mohallem, N. & Viana, M. M. 2022 Ag/GO/TiO2 nanocomposites: the role of the interfacial charge transfer for application in photocatalysis. *Nanotechnology* **33**, 035710 (9pp).

Bian, Z., Tachikawa, T., Zhang, P., Fujitsuka, M. & Majima, T. 2014 Au/TiO_2 superstructure-based plasmonic photocatalysts exhibiting efficient charge separation and unprecedented activity. *Journal of the American Chemical Society* **136**, 458–465.

Carrara, S. 2020 Reactor ageing and phase-out policies: global and regional prospects for nuclear power generation. *Energy Policy* **147**, 111834.

Chen, C., Xun, L., Zhang, P., Zhang, J. & Tian, B. 2019 Z-scheme structure Sns2–Au–CdS with excellent photocatalytic performance for simultaneous removal of Cr(VI) and methyl orange. *Research on Chemical Intermediates* **45**, 3513–3524.

Dai, Z., Zhen, Y., Sun, Y., Li, L. & Ding, D. 2021 ZnFe2O4/g-C3N4 S-scheme photocatalyst with enhanced adsorption and photocatalytic activity for uranium(VI) removal. *Chemical Engineering Journal* **415**, 129002.

Guo, X., Hao, C., Jin, G., Zhu, H. Y. & Guo, X. Y. 2013 Copper nanoparticles on graphene support: an efficient photocatalyst for coupling of nitroaromatics in visible light. *Angewandte Chemie International Edition* **53**, 1973–1977.

Guo, Y., Li, L., Li, Y., Li, Z., Wang, X. & Wang, G. 2016 Adsorption and photocatalytic reduction activity of uranium(VI) on zinc oxide/rectorite composite enhanced with methanol as sacrificial organics. *Journal of Radioanalytical and Nuclear Chemistry* **310**, 883–890

Guo, Y., Guo, Y., Wang, X., Li, P., Kong, L., Wang, G., Li, X. & Liu, Y. 2017 Enhanced photocatalytic reduction activity of Uranium(VI) from aqueous solution using Fe_2O_3-Graphene oxide nanocomposite. *Dalton Transactions*. doi:10.1039.C7DT02639 K.

Han, X., Wang, Y., Cao, X., Dai, Y., Liu, Y., Dong, Z., Zhang, Z. & Liu, Y. 2019 Adsorptive performance of ship-type nano-cage polyoxometalates for U(VI) in aqueous solution. *Applied Surface Science* **484**, 1035–1040.

Heshmati, H., Torab-Mostaedi, M., Ghanadzadeh Gilani, H. & Heydari, A. 2014 Kinetic, isotherm, and thermodynamic investigations of uranium(VI) adsorption on synthesized ion-exchange chelating resin and prediction with an artificial neural network. *Desalination & Water Treatment* **55**, 1076–1087.

Ingram, D. B. & Linic, S. 2011 Water splitting on composite plasmonic-metal/semiconductor photoelectrodes: evidence for selective plasmon-induced formation of charge carriers near the semiconductor surface. *Journal of the American Chemical Society* **133**, 5202–5205.

Jiang, X.-H., Xing, Q.-J., Luo, X.-B., Li, F., Zou, J.-P., Liu, S.-S., Li, X. & Wang, X.-K. 2018 Simultaneous photoreduction of Uranium(VI) and photooxidation of Arsenic(III) in aqueous solution over g-C3N4/TiO2 heterostructured catalysts under simulated sunlight irradiation. *Applied Catalysis B: Environmental* **228**, 29–38.

Khorsandi, H., Teymori, M., Aghapour, A. A., Jafari, S. J. & Bargeshadi, R. 2019 Photodegradation of ceftriaxone in aqueous solution by using UVC and UVC/H2O2 oxidation processes. *Applied Water Science* **9**, 81.

Lassoued, A., Lassoued, M. S., Dkhil, B., Ammar, S. & Gadri, A. 2018 Photocatalytic degradation of methylene blue dye by iron oxide (alpha-Fe2O3) nanoparticles under visible irradiation. *Journal of Materials Science Materials in Electronics* **29**, 8142–8152.

Li, Y. & Ding, Y. 2010 Porous AgCl/Ag nanocomposites with enhanced visible light photocatalytic properties. *The Journal of Physical Chemistry C* **114**, 3175–3179.

Li, P., Wang, J., Wang, Y., Liang, J., He, B., Pan, D., Fan, Q. & Wang, X. 2019 Photoconversion of U(VI) by TiO_2: an efficient strategy for seawater uranium extraction. *Chemical Engineering Journal* **365**, 231–241.

Linic, S., Christopher, P. & Ingram, D. B. 2011 Plasmonic-metal nanostructures for efficient conversion of solar to chemical energy. *Nat Mater* **10**, 911–921.

Link, S., Christopher, P. & Ingram, D. B. 2011 Plasmonic-metal nanostructures for efficient conversion of solar to chemical energy. *Nature Materials* **10**, 911.

Litter, M. I. 2017 Last advances on TiO_2 -photocatalytic removal of chromium, uranium and arsenic. *Current Opinion in Green and Sustainable Chemistry* **6**, 150–158.

Liu, J., Yang, S., Wu, W., Tian, Q., Cui, S., Dai, Z., Ren, F., Xiao, X. & Jiang, C. 2015 3D flowerlike α-Fe_2O_3@ TiO_2 core–shell nanostructures: general synthesis and enhanced photocatalytic performance. *ACS Sustainable Chemistry & Engineering* **3**, 2975–2984.

Liu, C., Hsu, P. C., Xie, J., Zhao, J., Wu, T., Wang, H., Liu, W., Zhang, J., Chu, S. & Cui, Y. 2017a A half-wave rectified alternating current electrochemical method for uranium extraction from seawater. *Nature Energy* **2**, 17007.

Liu, J., Tian, Q., Wu, Z., Yao, W., Xiao, X. & Wu, W. 2017b Synthesis and photocatalytic application of trinary structural g-C3N4/Ag/Ag3PO4 composite nanomaterials. *Journal of Environmental Chemical Engineering* **5**, 5777–5785.

Liu, J., Wu, Z., He, Q., Tian, Q., Wu, W., Xiao, X. & Jiang, C. 2019 Catalytic application and mechanism studies of argentic chloride coupled Ag/Au hollow heterostructures: considering the interface between Ag/Au bimetals. *Nanoscale Research Letters* **14**, 35.

Liu, J., Ma, N., Wu, W. & He, Q. 2020 Recent progress on photocatalytic heterostructures with full solar spectral responses. *Chemical Engineering Journal* **393**, 124719.

Liu, Y., Wu, S., Liu, J., Xie, S. & Liu, Y. 2021 Synthesis of g-C3N4/TiO_2 nanostructures for enhanced photocatalytic reduction of U(vi) in water. *RSC Advances* **11**, 4810–4817.

Lu, C., Chen, R., Wu, X., Fan, M., Liu, Y., Le, Z., Jiang, S. & Song, S. 2016 Boron doped g-C3N4 with enhanced photocatalytic UO22+ reduction performance. *Applied Surface Ence* **360**, 1016–1022.

Lu, C., Zhang, P., Jiang, S., Wu, X., Song, S., Zhu, M., Lou, Z., Li, Z., Liu, F. & Liu, Y. 2017 Photocatalytic reduction elimination of UO22+ pollutant under visible light with metal-free sulfur doped g-C3N4 photocatalyst. *Applied Catalysis B Environmental* **200**, 378–385.

Ma, T., Wu, J., Mi, Y., Chen, Q., Ma, D. & Chai, C. 2017 Novel Z-Scheme g-C3N4/C@Bi2MoO6 composite with enhanced visible-light photocatalytic activity for beta-naphthol degradation. *Separation and Purification Technology* **183**, 54–65.

Mao, M., Zhao, S., Chen, Z., She, X., Yi, J., Xia, K., HuI, X., He, M. & Li, H. 2018 Designing all-solid-state Z-Scheme 2D g-C_3N_4/Bi_2WO_6 for improved photocatalysis and photocatalytic mechanism insight. *Green Energy & Environment* **3**, 229–238.

Ping, L., Wang, J., Wang, Y., Liang, J. & Fan, Q. 2019 An overview and recent progress in the heterogeneous photocatalytic reduction of U(VI). *Journal of Photochemistry and Photobiology C Photochemistry Reviews* **41**, 100320.

Tada, H., Ishida, T., Takao, A. & Ito, S. 2004 Drastic enhancement of TiO2-Photocatalyzed reduction of nitrobenzene by loading Ag clusters. *Langmuir* **20**, 7898–7900.

Taghipour, S., Hosseini, S. M. & Ataie-Ashtiani, B. 2019 Engineering nanomaterials for water and wastewater treatment: review of classifications, properties and applications. *New Journal of Chemistry* **43**, 7902–7927.

Tian, N., Huang, H., He, Y., Guo, Y., Zhang, T. & Zhang, Y. 2015 Mediator-free direct Z-scheme photocatalytic system: BiVO4/g-C3N4 organic-inorganic hybrid photocatalyst with highly efficient visible-light-induced photocatalytic activity. *Dalton Transactions* **44**, 4297–4307.

Tong, L., Zhu, T. & Liu, Z. 2011 Approaching the electromagnetic mechanism of surface-enhanced Raman scattering: from self-assembled arrays to individual gold nanoparticles. *Chemical Society Reviews* **40**, 1296–1304.

Torkabad, M. G., Keshtkar, A. R. & Safdari, S. J. 2017 Comparison of polyethersulfone and polyamide nanofiltration membranes for uranium removal from aqueous solution. *Progress in Nuclear Energy* **94**, 93–100.

Wang, Y., Liu, X., Zheng, C., Li, Y., Jia, S., Li, Z. & Zhao, Y. 2018 Tailoring TiO_2 nanotube-interlaced graphite carbon nitride nanosheets for improving visible-light-driven photocatalytic performance. *Advanced Science* **5**, 1700844.

Wang, Q., Gao, Q., Al-Enizi, A. M., Nafady, A. & Ma, S. 2020 Recent advances in MOF-based photocatalysis: environmental remediation under visible light. *Inorganic Chemistry Frontiers* **7**, 300–339.

Wen, J., Xie, J., Chen, X. & Xin, L. 2017 A review on g-C-based photocatalysts. *Applied Surface Science* **391**, 72–123.

Wu X. Z. L., Xia, D. & Chen, T. 2013 *Ag-g-C3N4 /TiO2 photocatalyst prepared by ultrasonic mixing method*. China patent application.

Xu, Y., Mo, Y., Tian, J., Wang, P., Yu, H. & Yu, J. 2016 The synergistic effect of graphitic N and pyrrolic N for the enhanced photocatalytic performance of nitrogen-doped graphene/TiO_2 nanocomposites. *Applied Catalysis B Environmental An International Journal Devoted to Catalytic Science & Its Applications* **181**, 810–817.

Yi, J., She, X., Song, Y., Xu, H., Zhang, P., Mo, Z., Liu, L., Du, D. & Li, H. 2016 A silver on 2D white-C3N4 support photocatalyst for mechanistic insights: synergetic utilization of plasmonic effect for solar hydrogen evolution. *RSC Advances* **6**, 112420–112428.

Yu, J., Low, J., Xiao, W., Zhou, P. & Jaroniec, M. 2014 Enhanced photocatalytic CO_2-Reduction activity of anatase TiO_2 by Coexposed {001} and {101} Facets. *Journal of the American Chemical Society* **136**, 8839–8842.

Yuan, Y., Feng, S., Feng, L., Yu, Q. & Wang, N. 2020 A Bio-inspired nano-pocket spatial structure for targeting uranyl capture. *Angewandte Chemie International Edition* **59**, 4262–4268.

Zhang, L., Li, H., Li, L., Deng, J., Deng, W. & Zhao, Y. 2013 Photocatalytic reduction of uranyl ions over anatase and rutile nanostructured TiO2. *Chemistry Letters* **42**, 689–690.

Zhou, J., Ren, F., Zhang, S., Wu, W., Xiao, X., Liu, Y. & Jiang, C. 2013 SiO2-Ag-SiO2-TiO2 multi-shell structures: plasmon enhanced photocatalysts with wide-spectral-response. *Journal of Materials Chemistry A* **1**, 13128–13138.

Zhu, C., Zhang, L., Jiang, B., Zheng, J., Hu, P., Li, S., Wu, M. & Wu, W. 2016 Fabrication of Z-scheme Ag3PO4/MoS2 composites with enhanced photocatalytic activity and stability for organic pollutant degradation. *Applied Surface Ence* **377**, 99–108.

First received 10 February 2022; accepted in revised form 13 April 2022. Available online 26 April 2022